Chinese Journal of Chemical Engineering 82 (2025) 138–152

Contents lists available at ScienceDirect

Chinese Journal of Chemical Engineering

journal homepage: www.elsevier.com/locate/CJChE

Full Length Article

Numerical simulation of circulating fluidization roasting desulfurization of high-sulfur bauxite based on computational particle fluid dynamics method

Langfeng Fan [1,2], Chengming Xie [1,2], Qijin Wei [3], Hongliang Zhao [1,2,*], Rongbin Li [1,2], Yongmin Zhang [4], Fengqin Liu [1,2], Hong Yong Sohn [5]

[1] State Key Laboratory of Advanced Metallurgy, University of Science and Technology Beijing, Beijing 100083, China
[2] School of Metallurgical and Ecological Engineering, University of Science and Technology Beijing, Beijing 100083, China
[3] BGRIMM Technology Group, Beijing 100160, China
[4] State Key Laboratory of Heavy Oil Processing, China University of Petroleum, Beijing 102249, China
[5] Department of Materials Science and Engineering, The University of Utah, Salt Lake City, UT 84112, USA

ARTICLE INFO

Article history:
Received 15 November 2024
Received in revised form
18 January 2025
Accepted 20 January 2025
Available online 8 March 2025

Keywords:
Fluidization
Circulating fluidized bed
Numerical simulation
CPFD method
Roasting desulfurization
Bauxite

ABSTRACT

As a pyrometallurgical process, circulating fluidized bed (CFB) roasting has good potential for application in desulfurization of high-sulfur bauxite. The gas–solid distribution and reaction during CFB roasting of high-sulfur bauxite were simulated using the computational particle fluid dynamics (CPFD) method. The effect of primary air flow velocity on particle velocity, particle volume distribution, furnace temperature distribution and pressure distribution were investigated. Under the condition of the same total flow of natural gas, the impact of the number of inlets on the desulfurization efficiency, atmosphere mass fraction distribution and temperature distribution in the furnace was further investigated.

1. Introduction

Complex bauxite such as the high-iron and high-sulfur bauxite [1] has a high-sulfur content, low aluminum–silicon ratio, and other impurities, resulting in serious corrosion of equipment, high mineral/alkali consumption, and low-quality alumina. Such a raw material is difficult to treat by the traditional Bayer process [2]. This type of mineral must undergo desulfurization treatment before it is used in alumina production. The current desulfurization treatment methods include flotation [3,4], roasting [5,6], precipitation method [7], and microbial method [8].

Compared with the flotation method, the precipitation method and the microbial method, the roasting method has a number of significant advantages, the roasting method can not only eliminate the sulfur, but also the roasted minerals have improved properties with respect to the subsequent dissolution, sedimentation and decomposition processes [9]. After the bauxite is roasted, the ore contains increased amounts of internal pores and cracks [10], which can speed up the ore dissolution rate. In addition, the red mud in the roasted ore is loose and porous, which accelerates the agglomeration of red mud particles, strengthens its adsorption capacity of flocculant, and improves the sedimentation performance [9].

The traditional rotary kiln roasting desulfurization [11], static roasting desulfurization [12], and gaseous suspension roasting [13] have the problems of a high roasting temperature, long roasting time, poor dissolution performance of bauxite after roasting, and high energy consumption. Therefore, the application of circulating fluidized bed (CFB) roasting [14] is proposed in this work. The fluidized particles are in a state of strong turbulence, and there is an asynchronous motion between fluid and particle phases, which thus leads to a constant renewal of the contact surface between the two, and strengthens the heat and mass transfer between the two phases [15]. The efficiency of the production device becomes higher due to the increase of the reaction contact area and the intensification of the transfer process. The CFB combustion technology has

* Corresponding author. State Key Laboratory of Advanced Metallurgy, University of Science and Technology Beijing, Beijing 100083, China.
E-mail address: zhaohl@ustb.edu.cn (H. Zhao).

https://doi.org/10.1016/j.cjche.2025.01.007

been widely used in industries such as metallurgy, power generation, mineral processing, and chemical engineering [16], and this method has the advantages of controllable material circulation, good thermal stability in the furnace and a more long-lasting furnace lining. The device is simple, the investment is low, and the production can be flexibly controlled [17].

The CFB roasting process is complex, and it is extremely difficult to analyze the chemical reaction, the gas–solid flow characteristics, and the mass and heat transfer due to the invisibility of the fluidized bed at high temperature. However, the roasting process inside the CFB can be visualized with the help of numerical simulation, which is conducive to deepening the study on convective patterns, combustion efficiency, particle and atmosphere distribution inside the roaster. In recent years, there has been an increasing number of studies on the numerical simulation of CFB using the computational particle fluid dynamics (CPFD) method. The CPFD method [18,19], which draws on the multiphase particle-in-cell method [20] and enables the calculation of the gas–solid interaction problems, especially when the system has a large number of solid particles [21], is ideally suited for simulation of industrial-scale fluidized beds. Shen *et al.* [22] used CPFD method to study the gas–solid flow and residual carbon in a 350 MW CFB boiler at different loads. Yan *et al.* [23] used CPFD method to investigate the effect of wind–coal distribution on the combustion in the furnace of a 600 MW supercritical CFB boiler at different loads. Chang *et al.* [24] used the CPFD method to investigate the effects of primary airflow and pulverized coal size on NO_x emissions and furnace performance of a 220 $t\cdot h^{-1}$ industrial CFB roaster, Liu *et al.* [25] studied the effects of secondary airflow on the combustion characteristics and NO emissions of a 440 $t\cdot h^{-1}$ boiler, and Zhang *et al.* [26] investigated the 75 $t\cdot h^{-1}$ biomass CFB boiler using the CPFD method to investigate the effect of the internal gas–solid flow and combustion characteristics as well as the secondary air arrangement on the CO gas emissions. All the above studies have verified the feasibility of using the CPFD method for the simulation of CFB. Meanwhile, they also indicate that the setting of operating parameters such as primary air and secondary air will have a significant impact on the operation of CFB.

Currently, the research on desulfurization in the CFB roasting process is very limited, and there is even less research on the setting of operating parameters. In order to reveal the distribution of the gas–solid field inside the roasting furnace and obtain the parameter settings of the primary air and natural gas inlets under the optimal roasting desulfurization operating conditions, and to provide data references for subsequent research and optimization, we decide to use the CPFD method to simulate the desulfurization process of high-sulfur bauxite CFB roasting.

In this paper, the prototype CPFD model that has been established is a high-sulfur bauxite CFB roaster with a production capacity of 310 $t\cdot d^{-1}$ industrial grade. This study focuses on the atmosphere distribution in the furnace and the desulfurization efficiency. Firstly, the correctness of the CPFD numerical simulation method is verified, and then on this basis, the gas–solid flow characteristics during roasting are studied. Finally, the effects of the primary air flow velocity and the number of the natural gas inlets on the gas–solid flow, temperature field and atmosphere distribution in the furnace were investigated. The simulation work done in this paper addresses the gap in existing research on high-sulfur bauxite desulfurization through CFB roasting, providing a novel technical thought for desulfurizing high-sulfur bauxite.

2. CPFD Model

In this study, a three-dimensional model of the high-sulfur bauxite CFB roaster desulfurization process is established using the CPFD method. The radiative heat transfer, methane combustion, gas–solid two-phase flow, and high-sulfur bauxite desulfurization in the CFB roaster are numerically simulated.

2.1. Mathematical model

According to the CPFD simulation method, particle phase governing equation, the gas phase governing equation, mass transfer equation and heat transfer equation are mainly used in the simulation process.

In the current research on CFB using the CPFD method, the Wenyu–Ergun model is mainly adopted as the drag model [22–29]. This model combines the Wenyu drag model and the Ergun drag model by adding a transition function, and it can calculate the resistance when the particle volume concentration is between 0 and 0.7. It is applicable to CFB systems with both dense and dilute phases. Therefore, the Wenyu–Ergun drag model will be used for calculations in this research.

The governing equations used in the simulation process in more detail are displayed in Table 1.

2.2. Chemical reaction model

In Barracuda, the method of cell-average chemistry calculation is used. This method interpolates the properties of discrete particles into a grid cell to calculate the average properties of the particle phase, which is used to calculate the rate of a chemical reaction [36]. The software uses stoichiometric equations to control material balances and power-law rate laws to calculate reaction rates, both of which combine to form the reaction module, and the Arrhenius equation is mainly used to calculate chemical reaction rate constants:

$$k = A_0 m_s^{C_1} T^{C_2} \exp\left(-\frac{E}{RT} + E_0\right)$$

During desulfurization of high-sulfur bauxite by circulating fluidized roasting, in addition to the desulfurization reaction, the following reactions can also occur: gas combustion and dehydration of diaspore monohydrate. The relevant chemical reaction kinetic parameters are shown in Table 2 [24,43–45].

2.3. Modeling, boundary conditions, and meshing

The simulated system is a 310 $t\cdot d^{-1}$ CFB roaster, which mainly consists of main roasting furnace, cyclone separator and return valve. The relevant dimensions of each part are shown in Fig. 1(a), the cyclone separator exhaust port is set as the pressure outlet, the bottom of the main furnace and the return valve are set as the flow inlet, and a ring of 8 jet nozzles arranged at 45° downwards is set at the cone 1.45 m from the bottom of the main furnace. At the same time, a gas distribution plate is provided to evenly distribute the gas in the furnace, with 1020 small holes of a radius of 2.5 mm. These small holes are grouped such that every 6 of them are evenly distributed on one of the 170 hoods, which are radially distributed on the plate. The gas distribution plate is shown in Fig. 1(b). In order to be realistic and close to industrial production, the CFB roaster was modeled in 1:1 3D, and the full cycle simulation was carried out to reduce the error.

Fig. 2 shows meshing. By using Barracuda's own Baffles function, the three-dimensional gas distribution plate is treated as a shell structure consisting of surfaces and the passage probability of particles and gases is adjusted to 0, which acts as a deterrent. This effectively avoids the division of a fine mesh while at the same time realizing the function of the gas distribution plate.

Table 1
Governing equations in numerical simulations.

Equation	Number
Gas-phase governing equations	
Continuity equation [30,31]	
$\frac{\partial(\theta_f \rho_f)}{\partial t} + \nabla\cdot(\theta_f \rho_f \boldsymbol{u}_f) = \delta \dot{m}_p$	(1)
Momentum equation	
$\frac{\partial \theta_f \boldsymbol{u}_f}{\partial t} + \nabla\cdot(\theta_f \boldsymbol{u}_f \boldsymbol{u}_f) = -\frac{1}{\rho_f}\nabla P - \frac{1}{\rho_f}\boldsymbol{F} + \theta_f \boldsymbol{g} + \frac{1}{\rho_f}\nabla \boldsymbol{\tau}_f$	(2)
Momentum exchange frequency	
$\boldsymbol{F} = \iint f_m \left[D_P(\boldsymbol{u}_f - \boldsymbol{u}_p) - \frac{\nabla P}{\rho_p}\right] \mathrm{d}m \mathrm{d}\boldsymbol{u}_p$	(3)
Energy equation [32,33]	
$\frac{\partial(\theta_f \rho_f h_f)}{\partial t} + \nabla\cdot(\theta_f \rho_f h_f \boldsymbol{u}_f) = \theta_f\left(\frac{\partial P}{\partial t} + \boldsymbol{u}_f \cdot \nabla P\right) + \phi + Q + S_h + q_D + \nabla\cdot(\theta_f k_f \nabla T_f)$	(4)
Governing equations of particle phase	
Particle phase momentum equation [31,34]	
$\frac{d\boldsymbol{u}_p}{dt} = D_P(\boldsymbol{u}_f - \boldsymbol{u}_p) - \frac{1}{\rho_f}\nabla P + \boldsymbol{g} - \frac{1}{\theta_p \rho_p}\nabla \tau_p + \boldsymbol{F}_p$	(5)
Normal stress [35,36]	
$\tau_p = \frac{10 P_S \theta_p^{\beta}}{\max[(\theta_{cp} - \theta_p), \varepsilon(1-\theta_p)]}$	(6)
Particle energy equation [32,33]	
$c_V \frac{\mathrm{d}T_p}{\mathrm{d}t} = \frac{A_p}{m_p} h_p (T_f - T_p) + \frac{1}{m_p} H_{fp}^{C}$	(7)
Drag coefficient	
$D_P = f_d \frac{3}{8} \frac{\rho_f}{\rho_p} \frac{\lvert \boldsymbol{u}_f - \boldsymbol{u}_p \rvert}{r_p}$	(8)
Wenyu–Ergun model [37]	
$f_{w-e} = \begin{cases} f_w, \ \theta_p < 0.75\theta_{CP} \\ f_w + \frac{\theta_p - 0.75\theta_{CP}}{0.1\theta_{CP}}, \ 0.75\theta_{cp} < \theta_p < 0.85\theta_{CP} \\ f_e, \ 0.85\theta_{CP} < \theta_p \end{cases}$	(9)
Reynolds number equation	
$Re = \frac{2\rho_f r_p \lvert \boldsymbol{u}_f - \boldsymbol{u}_p \rvert}{\mu_f}$	(10)
Heat transfer equations	
Radiative heat transfer equation [38]	
$q_{WP} = A_W F_{WP} \varepsilon_{WP} \sigma_{WP} (T_W^4 - T_P^4)$	(11)
Heat transfer equation between fluid and walls [39]	
$h_{fw} = h_l + f_d h_d$	(12)
$f_d = 1 - e^{-10\left(\frac{\theta_p}{\theta_{CP}}\right)}$	(13)
Lean phase heat transfer coefficient equation	
$h_l = (c_0 Re_L^{n_1} Pr^{n_2} + c_1)\frac{k_f}{L} + c_2$	(14)
Dense phase heat transfer coefficient equation	
$h_d = c_0 Re_p^{n_1} \frac{k_f}{d_p}$	(15)
Heat transfer equation between fluid and particles [40]	
$h_p = \frac{\left(c_0 Re_p^{n_1} Pr^{0.33} + c_1\right) k_f}{d_p} + c_2$	(16)
Transport equation [41,42]	
$\frac{\partial(\theta_f \rho_f Y_{f,i})}{\partial t} + \nabla\cdot(\theta_f \rho_f Y_{f,i} \boldsymbol{u}_f) = \nabla\cdot(\rho_f D \theta_f \nabla Y_{f,i}) + \delta \dot{m}_{i,chem}$	(17)

Tables 3 and 4 show the basic parameter settings for the simulation in the Barracuda simulation.

In the first 0.5 s of the calculation, a time step of 0.0001 s was set to ensure the stability of the calculation. From 0.5 to 1 s, the time step was set to 0.001 s. After the calculation gradually stabilized, in order to improve the calculation efficiency, a time step of 0.01 s was set to continue the calculation until 120 s. The roaster is filled with 873 K air, at the same time, the roaster is equipped with 8500 kg of bed material at a temperature of 950 K, and other initial boundary conditions are given in Tables 3 and 4. Primary air, natural gas and fluidized air inlets are designated as flow boundary condition (BC), and flue gas outlets are designated as pressure BC. For industrial-scale plants, such as [47–49] system, heat loss is kept to a very low percentage. Therefore, the heat exchange between the roaster and the outside is not considered in the simulation process.

Table 5 shows the size distribution of particles used, and a particle layer with an initial height of 0.850 m is present in the furnace.

2.4. Grid independence verification

Before using Barracuda for simulation, grid independence verification is performed first. And the thermal state simulation was carried out with coarse grids (212000), medium grids (407154), fine grids (612900) to monitor the temperature distribution of main furnace. Fig. 3 shows that the 212000 grid temperature distribution fluctuates greatly. When the number of grids increases from 407154 to 612900 grids, the temperature distribution is relatively more stable, and the simulation results are less related to the number of grids. Both the medium grids and the fine grids meet the requirements of the simulation. However, considering the computational time together with solution accuracy, the mesh size of 407154 cells was selected for this work.

2.5. Model validation

To verify the feasibility of the CPFD method in this study, a small test bench with the same structure as the real CFB roaster was built in this work at a scale ratio of 30:1. The validation experiments were set up with four different air inlet volumes. The particle flow field in the test bench running under different air inlet volumes was compared with that from the CPFD simulation under the same conditions, and the comparison diagrams are shown in Figs. 4 and 5. The colors in the simulation plot represent the values of the particle volume fraction. It can be clearly seen that the experimental results under four different air inlet velocities are very close to the simulation results under the same conditions. The maximum difference between the simulation result and the experimental height is 0.014 m, and the error is less than 10%. Further, given the reported studies [23–25,28,29,50] showing that the thermal models simulation of CFB reactor based on the CPFD method are all in good conformity with the real equipment. In summary, the CPFD model established in this paper is considered reliable and can be used in the next step of research.

3. Results and Analysis

3.1. The influence of the primary air flow velocity on the distribution of particle flow, pressure, temperature and field

The primary air flow velocity plays a key role in the gas–solid flow inside the furnace. Excessive primary air flow velocity leads to the disorder of the flow field distribution inside the roaster, which will lead to a poor reaction effect inside the furnace. If the primary air feed rate is insufficient it cannot support the circulating flow of the roaster. The primary air flow velocity also has a great influence on the pressure and temperature distribution in the furnace [51]. As thus, it is very important to select the appropriate primary air flow velocity to maintain the stability of production. The effect of the primary air flow velocity on the gas–solid phase in the furnace under the condition of ensuring smooth fluidization is discussed in this subsection. Keeping the excess air coefficient constant during simulation, the settings are shown in Table 6.

Fig. 6 shows the variation of the particle flow state inside the furnace over time for different primary air flow velocity. Within 0–20 s, the particles rapidly changed from the packed state to the fluidized state. Within 20–80 s, the particles continue to rise under

Table 2
Models of chemical reaction kinetics used.

Reactions		Rate equations	Rate constant
1	$H_2O(moisture) \rightarrow H_2O(g)$	$R_1 = k_1[H_2O]$	$k_1 = 5.13 \times 10^{10}\exp(-10585/T)$
2	$CH_4+2O_2 \rightarrow CO_2+2H_2O$	$R_2 = k_2[CH_4][O_2]$	$k_2 = 3.552 \times 10^{14}\exp(-15700/T)$
2	$2AlOOH \rightarrow Al_2O_3+H_2O$	$R_3 = k_3$	$k_3 = 1.78 \times 10^{11}\exp(-30615.8/T)$
4	$4FeS_2+11O_2 \rightarrow 2Fe_2O_3+8SO_2$	$R_4 = k_4[O_2]$	$k_4 = 1 \times 10^{14}\exp(-31180/T)$

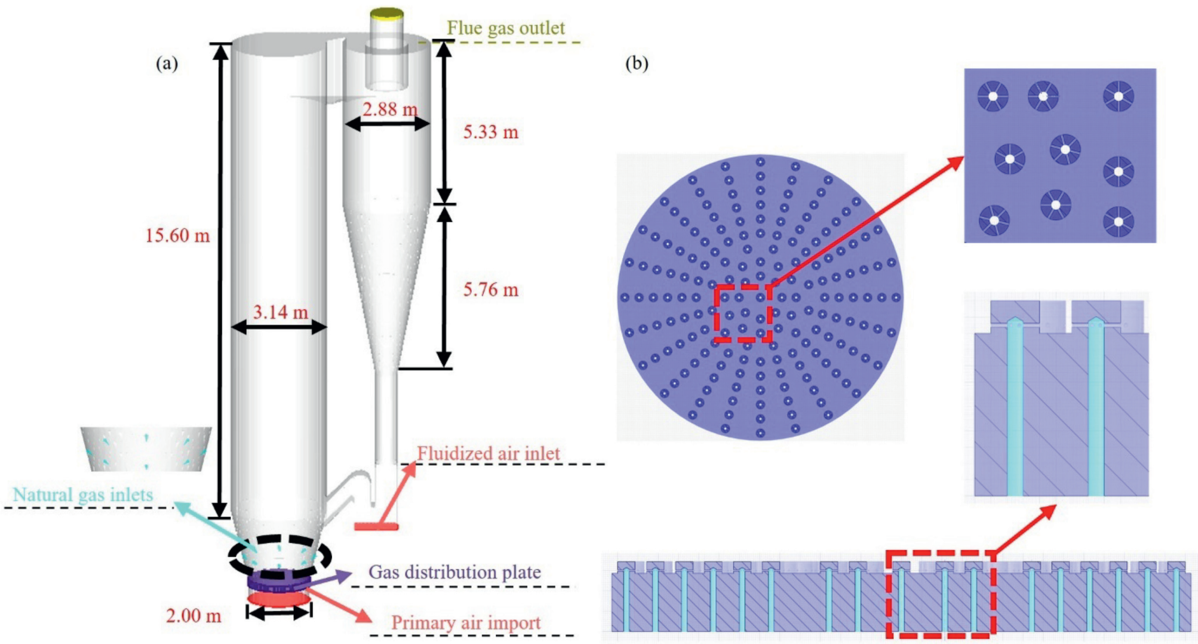

Fig. 1. Schematic of the geometric model: (a) CFB roaster and boundary conditions, (b) gas distribution plate.

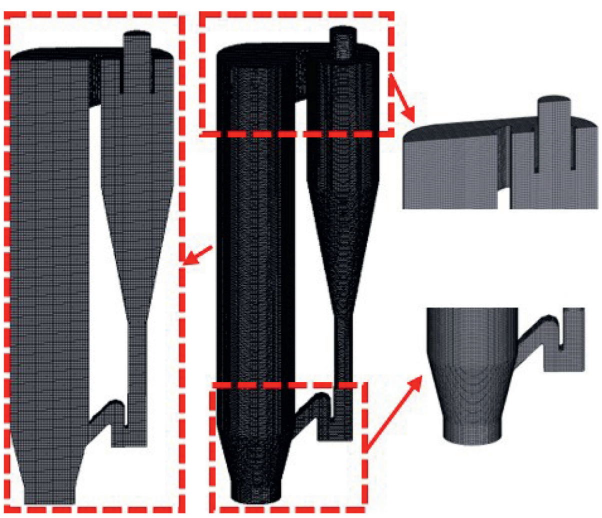

Fig. 2. Meshing.

Table 3
Basic parameter settings for the simulation [46].

Option	Parameter setting
Density of particles/kg·m^{-3}	3900
Initial mass of the material bed/kg	8500
Accumulation porosity of particles	0.63
Constant total air flow/m^3·s^{-1}	11.5
Normal-to-wall momentum retention	0.35
Tangent-to-wall momentum retention	0.995

Table 4
Parameters for thermal simulation.

Option	Parameter setting
Initial roaster temperature, except bed material/K	873
Temperature of initial bed particles/K	950
Temperature of natural gas, set as ignition temperature/K	900
Temperature of primary air/K	300
Temperature of fluidization air/K	300
Constant total natural gas flow/kg·s^{-1}	0.155
The flow of primary air/kg·s^{-1}	5.08
The flow of fluidization air/kg·s^{-1}	0.342

the drive of the airflow until they reach the top of the roasting main furnace and then are sent to the cyclone separator for gas—solid separation. The separated solid particles enter the return section *via* the leg of the cyclone separator, and then flow to the roasting main furnace under the action of the fluidized air of the return valve, so that the material reaches the CFB roasting state. Judging from the temperature change in Fig. 7 and the change in the particle accumulation height of the cyclone separator leg in Fig. 6, the gas—solid flow and combustion reaction tend to stabilize after 80 s.

From Fig. 7, it is seen that when the primary air flow velocity is 1.25 m·s^{-1} the particle fluidization rate is slower, and when the particle flow reaches a stable circulating flow state, there is a large number of particle accumulation at the bottom of the furnace, the

Table 5
Sample particle size distribution.

Diameter/μm	Mass proportion/%
>150	34.2
75–150	9.3
45–75	5.3
25–45	4.4
<45	46.8
Total	100.0

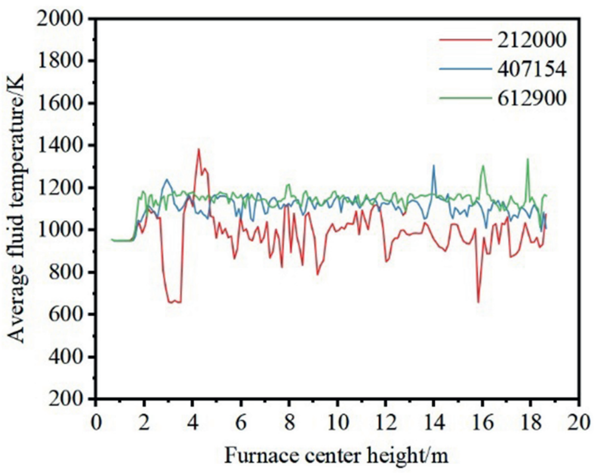

Fig. 3. The average fluid temperature distributions in the center of the furnace for different grid numbers.

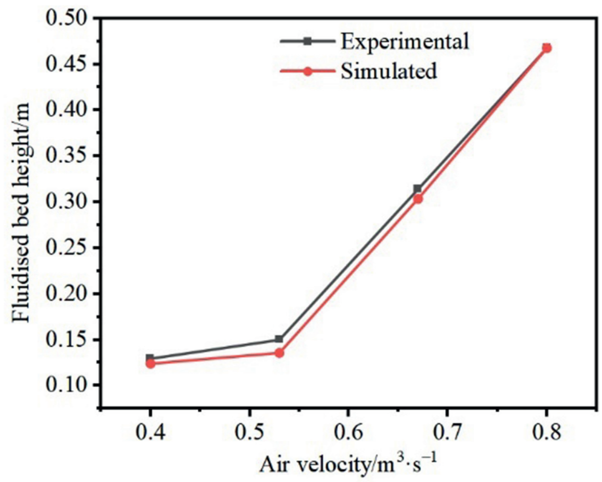

Fig. 5. Experimental and simulated fluidized bed heights at different air velocity.

accumulation is likely to cause circulating fluidization blockage of the system, which in turn affects the normal operation. When the flow velocity is 1.50 m·s^{-1}, the particle fluidization rate is moderate, and when the particles in the furnace reach stable circulating fluidization, the particles are evenly distributed and flow smoothly without blockage. When the primary air flow velocity is 1.75 m·s^{-1}, particles have maximum velocity, and when the particles in the furnace reach a stable circulating fluidization, a large number of particles enter the cyclone separator due to excessive primary air flow. However, the return rate has a certain limit, excessive

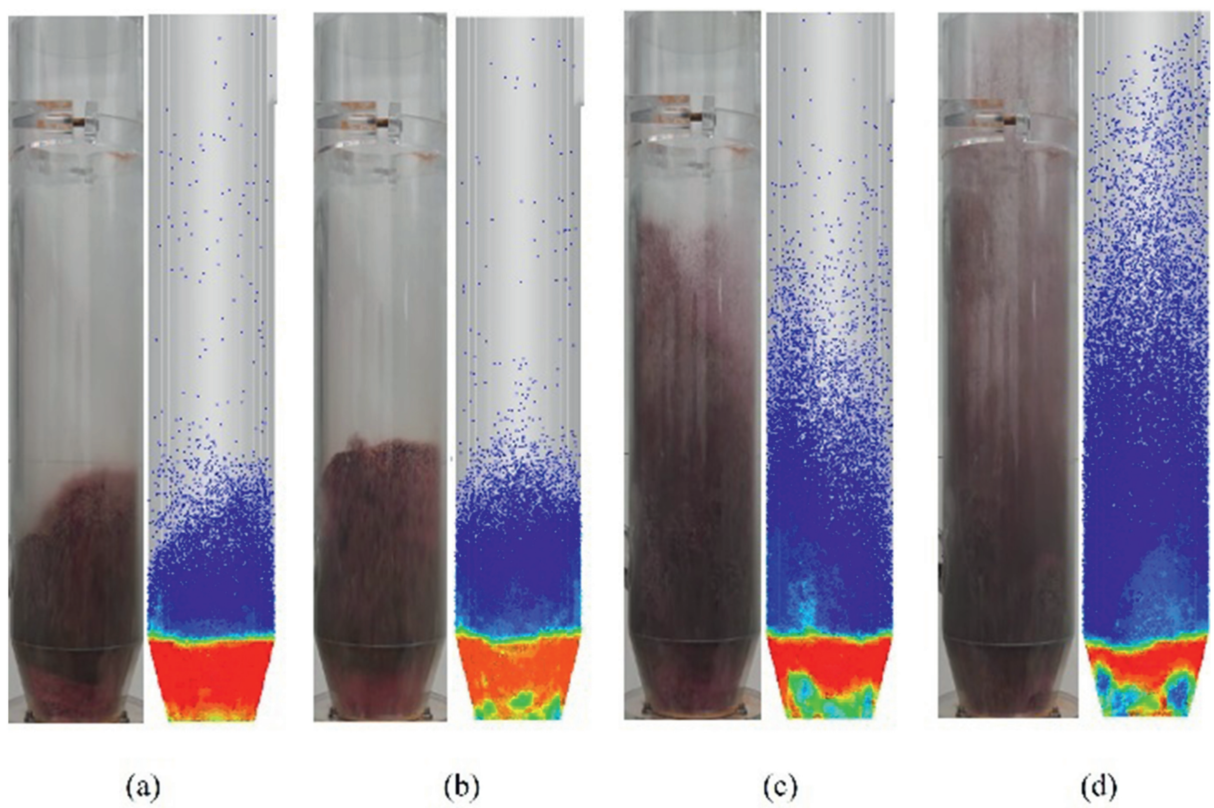

Fig. 4. Comparisons of experimental and simulated results when the airflow is (a) 0.4 m^3·s^{-1}, (b) 0.53 m^3·s^{-1}, (c) 0.67 m^3·s^{-1}, and (d) 0.8 m^3·s^{-1}.

Table 6
Parameters for different primary and natural gas feed rates with the same air excess coefficient.

Case	Primary air flow velocity/m·s^{-1}	Natural gas feed rate/kg·s^{-1}	Total air feed rate/kg·s^{-1}	Excess air coefficient
(a)	1.25	0.123	4.33	1.25
(b)	1.50	0.148	6.21	1.25
(c)	1.75	0.172	7.16	1.25

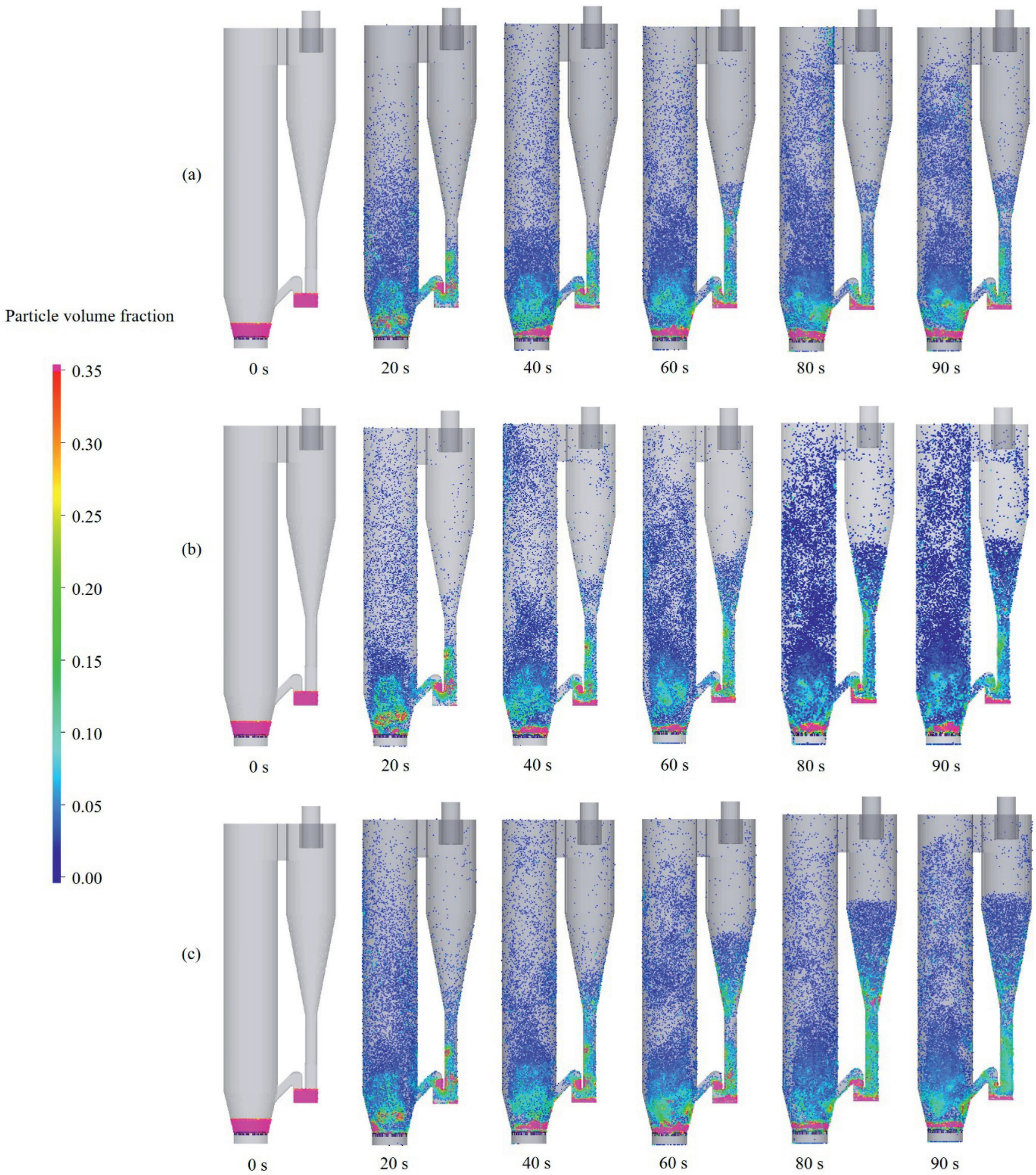

Fig. 6. The distributions of the volume fraction of particles in the roaster under different primary air flow velocities with the accompanying change in the total air feed rate: (a) 1.25 m·s^{-1}, (b) 1.50 m·s^{-1}, (c) 1.75 m·s^{-1}.

amounts of particles entering the cyclone legs will lead to blockage and unfavorable roasting and desulfurization conditions. It can be seen that, among the three primary air velocities under the simulation conditions in this paper, 1.50 m·s^{-1}, which is a moderate air velocity value, is more ideal for the stable operation of CFB roaster and the desulfurization of high sulfur bauxite.

Fig. 8 shows the particle velocity distributions at different heights in the vertical profile of the main roaster when the roaster

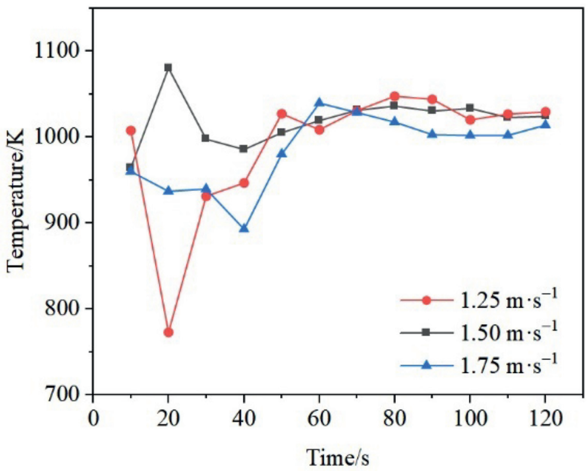

Fig. 7. The temperature at the bottom of the main furnace.

is operating stably. In the graph, an upward particle velocity is indicated as positive, and a downward particle velocity is indicated as negative. The “core–annular” pattern of particles as described by other researchers [52] is observed in the furnace. In this pattern, the particles are affected by the wall, resulting in the particles near the wall rising up slower and some of the particles moving downwards, the falling particle flow is called annular. While the particles away from the wall are less affected by the wall and rise more quickly, the upward gas–solid flow is called core. The whole furnace shows a flow of particles upward in the center and downward at the edges. The rising part of the particle flow in the center of the furnace moves downward along the wall to the bottom of the furnace under the obstruction of the wall, and then moves upward again under the drive of the central air flow.

Comparing Fig. 8(a), (b) and (c), it is evident that at the flow velocity of 1.25 $m\cdot s^{-1}$, the difference in particle velocity at different cross-section heights is small, and the velocity at the center of the cross-section is 1–3 $m\cdot s^{-1}$. In addition to the particles at the center of the cross-section moving upward, most of the particles are moving downward. The closer to the wall, the faster the particles move downward. The overall velocity of particles is relatively slow. At a primary air flow velocity of 1.50 $m\cdot s^{-1}$, the difference in particle velocity at different cross-section heights is small, and the velocity at the center of the cross-section is 2–6 $m\cdot s^{-1}$. A small portion of the particles near the wall move downward. At a primary air flow velocity of 1.75 $m\cdot s^{-1}$, there is a large difference in particle velocity at different cross-section heights, and the velocity at the center of the cross-section is 4–8 $m\cdot s^{-1}$. Most of the particles in the region move upward. The velocity gradient of the particles is large, and the overall velocity is fast. At this primary air flow velocity, the particles quickly enter the cyclone separator from the main furnace. This situation is not conducive to the effective roasting and desulfurization process of high-sulfur bauxite, and it also needs to

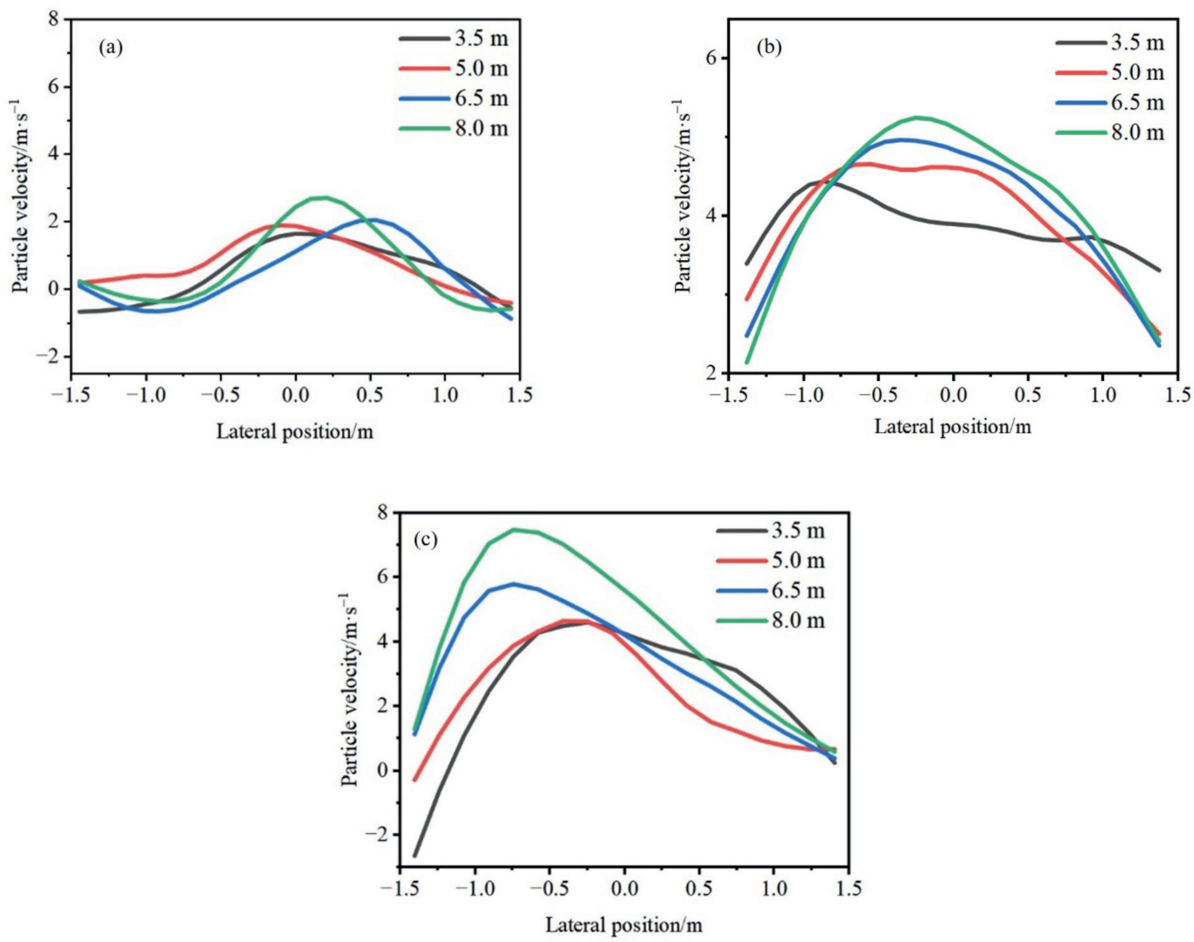

Fig. 8. Particle velocities at different cross-section heights for different primary air flow velocities: (a) 1.25 $m\cdot s^{-1}$, (b) 1.50 $m\cdot s^{-1}$, and (c) 1.75 $m\cdot s^{-1}$.

consume more fuel. It can be seen that the three primary air velocities under the simulated conditions in this paper, when the flow velocity is 1.50 $m \cdot s^{-1}$, the gas—solid flow state in main furnace is optimal, under this primary air flow the bauxite can be fully roasted and desulfurized.

Fig. 9 shows the pressure distribution in the roaster at different primary air flow velocities when the CFB roaster is running stably. The figures show high pressure values at the bottom of the CFB roaster and in the feeder, while the pressure at the exhaust outlet is the lowest, and the pressure increases with furnace height.

It can also be seen from the figure that the maximum values of the internal pressure of the furnace for the three operating conditions with primary air velocity increasing from low to high are 179, 182 and 184 kPa. There is a positive correlation between the maximum pressure and the flow velocity in the furnace, and the pressure of the cyclone separator leg and the return valve gradually increases as the primary air flow velocity increases. For the return valve, a certain pressure is required to promote the circulation of the material, but the excessive pressure accelerates the circulation rate of the material. At this point, too many particles enter the return valve, leading to the blockage of the return valve. Similarly, too small pressure slows down the circulation rate of the material, and more particles stay at the bottom of main furnace can likewise lead to localized blockages, which affects the normal operation of the roaster [53]. It is clear that, among the three primary air velocities under the simulated conditions in this paper, under a primary air flow velocity of 1.50 $m \cdot s^{-1}$, pressure distribution inside the furnace is more favorable for bauxite roasting and desulfurization.

Fig. 10 shows the temperature distribution in the roaster at different primary air flow velocities when the CFB roaster is running stably. As shown in Fig. 10, the bottom temperature of the roasting furnace is the lowest and the temperature distribution is uneven, the temperature in the middle and lower parts is the highest, and the temperature distribution in the middle and upper parts is very uniform radially. In the cyclone separator, the temperature gradually decreases from the flue gas outlet to the material leg, the temperature at the return valve is also lower. As can be seen from the horizontal plane of 3 m and 2.3 m in the figure, the temperature in the bottom area near the wall is higher than that in the center area. Fig. 10 show that the primary air flow velocity has little impact on the overall temperature distribution, but has a greater impact on the temperature distribution at the bottom of the roaster. Temperature distribution at the bottom of the furnace is more evenly distributed at the other two air velocities than at an air velocity of 1.50 $m \cdot s^{-1}$, because a small flow velocity causes more particles to stay in the lower part of the main furnace, and a larger flow velocity causes the air flow at the bottom to be disordered, which makes the temperature at the bottom of the roaster fluctuate greatly. At the three simulated flow velocities, under the primary air flow velocity of 1.50 $m \cdot s^{-1}$, the temperature distribution inside the furnace is even/homogeneous, which contributes to the desulfurization reaction of bauxite roasting.

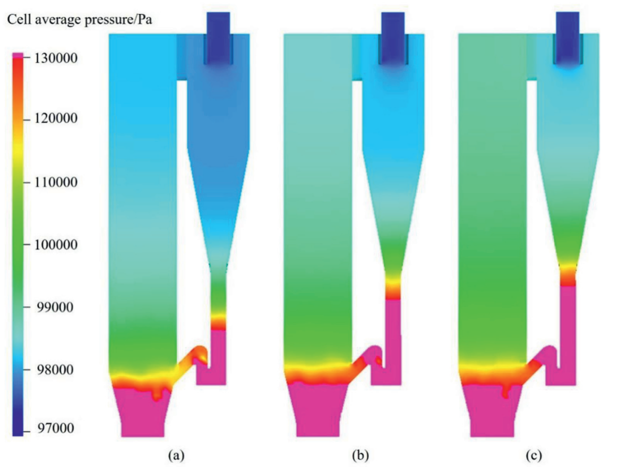

Fig. 9. Pressure distributions in the roaster under different primary air velocities: (a) 1.25 $m \cdot s^{-1}$, (b) 1.50 $m \cdot s^{-1}$, and (c) 1.75 $m \cdot s^{-1}$.

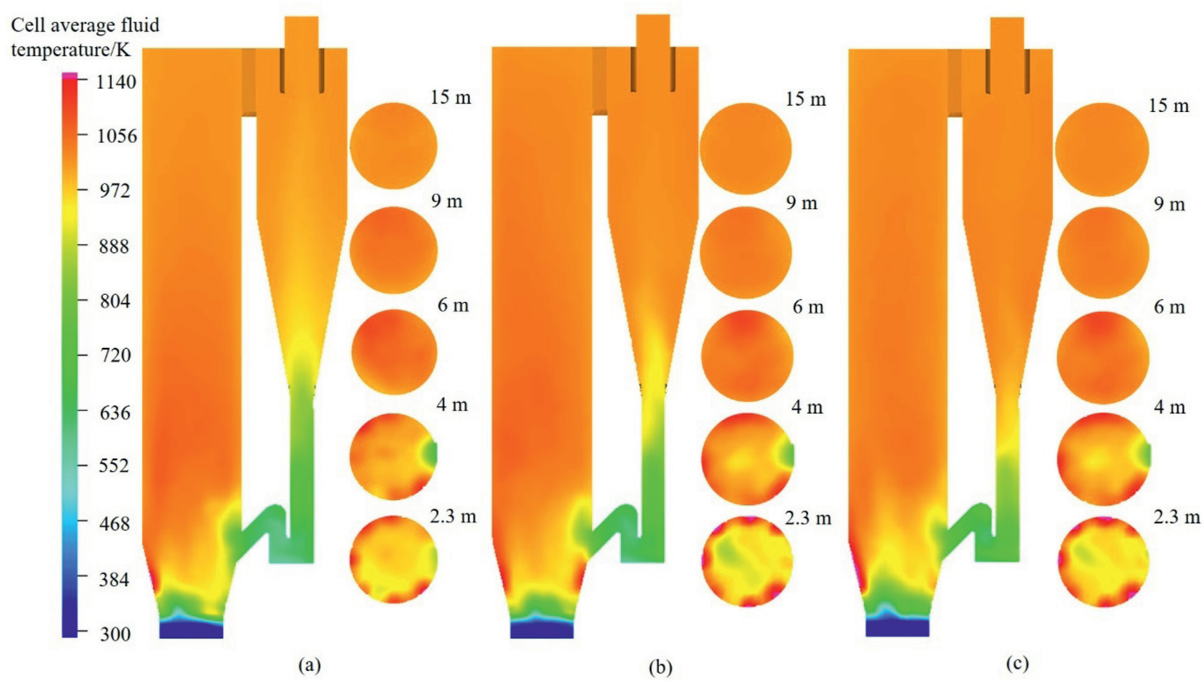

Fig. 10. Temperature distributions in the roaster under different primary air velocities: (a) 1.25 $m \cdot s^{-1}$, (b) 1.50 $m \cdot s^{-1}$, and (c) 1.75 $m \cdot s^{-1}$.

3.2. The influence of the number of natural gas inlets on the temperature field, gas distribution and desulfurization efficiency in the furnace

The natural gas enters the roaster at a fixed flow through the inlet to burn and produce heat. The number of natural gas inlets directly determines the velocity of the natural gas, and the velocity of the natural gas determines its penetration depth. The depth of penetration affects the uniformity of reactant mixing and thus affects the chemical reaction rate [54]. When the total flow is constant, the less the number of natural gas inlets, the faster the flow velocity and the deeper the penetration depth of natural gas. But excessive penetration hinders the primary air at the bottom of the main furnace to carry the solids up, weakening the degree of gas–solid mixing in the furnace and resulting in insufficient gas–solid reaction and combustion reaction [55,56]. Too many natural gas inlets lead to insufficient penetration of the natural gas into the bed material, so that the natural gas cannot fully contact the reactants in the center region of the furnace. In this case, the combustion efficiency and temperature will be reduced, and the desulfurization reaction efficiency will be reduced [57]. The right amount of natural gas inlets can contribute to reducing the energy consumption of roasters and facilitate the desulfurization of bauxite, reducing emissions of exhaust gas. In this section, under the premise that the smooth fluidization of materials is ensured and other conditions remain unchanged, the effects of the natural gas inlet number are discussed. The natural gas inlet is set up using Barracuda software's jet module, which simplifies the calculation and ensures the accuracy of the simulation. Fig. 11 shows the setting of the jet boundary conditions.

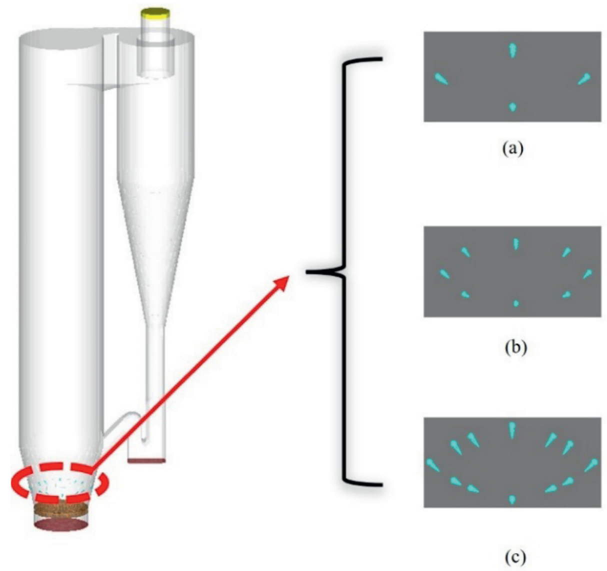

Fig. 11. Distributions and numbers of the natural gas inlets: (a) 4, (b) 8, and (c) 12.

Fig. 12 shows the distribution of the mass fraction of water vapor in the furnace with different numbers of natural gas inlets during stable operation of the CFB roaster. Simulation results in the figure show that mass fraction of water vapor is largest in the lower part of the main roasting furnace and smallest at the return valve and cyclone separator legs. The water vapor in the roaster is generated mainly by the combustion of natural gas and dehydration of diaspore monohydrate, the natural gas enters the combustion zone from the wall of the conical section at the bottom of the roaster, and a large amount of diaspore monohydrate is dehydrated at the bottom of the roaster in the concentrated phase area. In Fig. 13, for the 4 inlets, the peak of the water vapor mass fraction is narrow and sharp, with a peak value of 0.19, which is much higher than the peak values of the other two cases. This indicates that when the number of inlets is 4, the strong natural gas flow blocks the upward movement of the primary air and the solid particles carried by it, resulting in most of the material particles being gathered in the bottom. And the water vapor generated by the bauxite dehydration and combustion reaction is collected in this region. When the number of natural gas inlets is 8 and 12, the blocking effect of the natural gas is weakened. The primary air and the particles carried

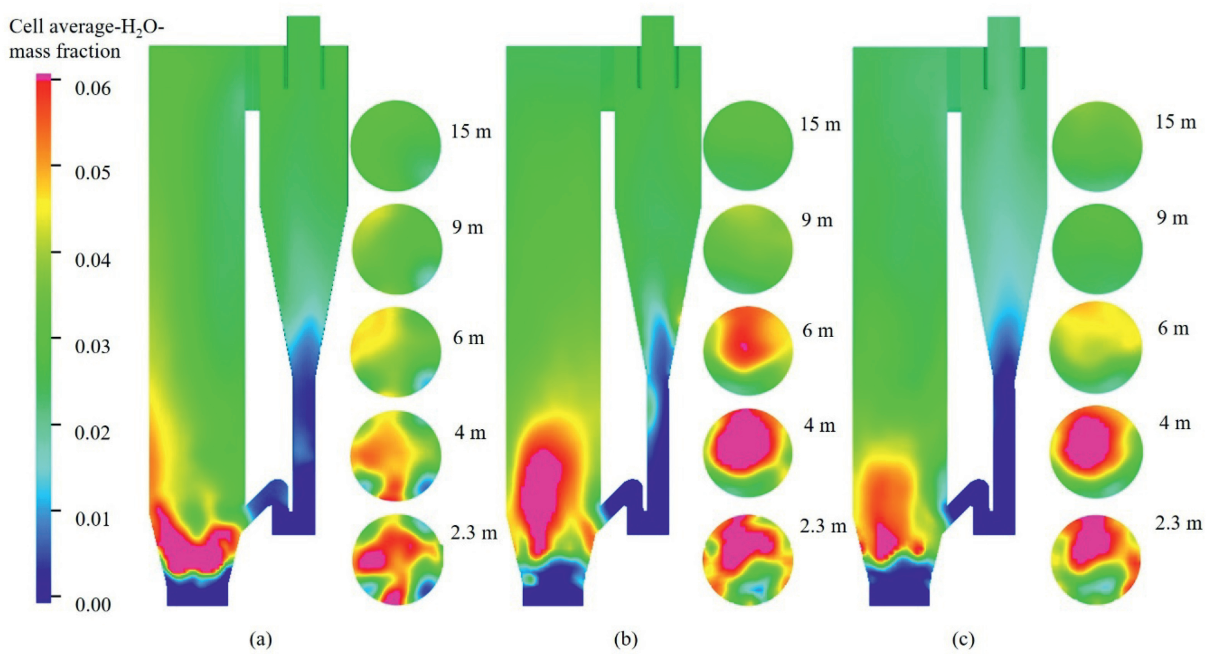

Fig. 12. Distributions of water vapor in the furnace under different natural gas inlet numbers: (a) 4, (b) 8, and (c) 12.

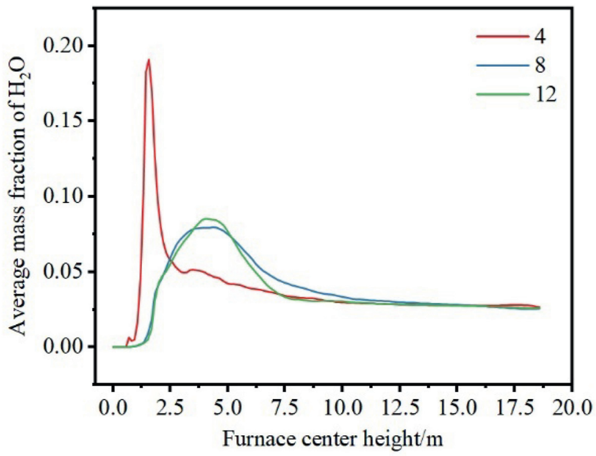

Fig. 13. Distributions of water vapor mass fraction at the center of CFB roaster for different numbers of natural gas inlets.

by it mix with the natural gas to form a wider reaction zone in the height direction. For the cases where the number of inlets is 8 and 12, the larger area shown in Fig. 12 and the wider peaks shown in Fig. 13 indicate that the area of reaction is larger for the number of inlets 8. This may be because with 8 natural gas inlets, the natural gas penetration ability is stronger than that with 12 inlets, and thus the gas—solid contact in the center area is more adequate. From the horizontal cross-section of 2.3—15 m in Fig. 12, it is also seen that when the number of natural gas inlets is 4, the reaction area is too concentrated, and the distribution of water vapor mass fraction under the action of the strong natural gas is in the shape of a cross. When the inlets are 8 and 12, the gas mixing and dispersion are in the shape of an ellipse.

Fig. 14 shows the distribution of the mass fraction of carbon dioxide in the furnace for different numbers of natural gas inlets during stable operation of the CFB roaster. Simulation results in the figure show that the mass fraction of carbon dioxide reaches maximum value in the lower part of the main furnace, and reaches minimum value at the legs of the return valve and cyclone separator. The carbon dioxide in the roaster is generated by the combustion of natural gas, which enters the combustion zone from the wall of the cone section at the bottom of the roaster. Similarly, Fig. 15 shows that when the number of natural gas inlets is 4, the combustion product CO_2 accumulates in the bottom region due to the barrier effect of the natural gas and the average local mass fraction of CO_2 increases to 0.047. Moreover, compared with the case where the number of inlets is 12, when the number of inlets is 8, the peak value of the mass fraction is larger, reaching 0.052. The mass fraction at height above 5.28 m is also greater than that when the number of inlets is 12. This means that the combustion reaction is relatively more complete at an inlet number of 8.

Fig. 16 shows the distribution of the oxygen mass fraction in the furnace with different numbers of natural gas inlets during stable operation of the CFB roaster. Simulation results in the figure show that except for the two inlets, there is more oxygen distribution at the legs of the cyclone. And the oxygen content is very small in the main roasting furnace and the upper part of the cyclone. In the main furnace, oxygen enters from the bottom of the inlet main furnace, mixes with natural gas in the main furnace cone to complete combustion, and some unreacted oxygen rises and diffuses to the upper part of the main furnace, resulting in the oxygen in the main furnace showing the curve of Fig. 17, which is decreasing and then increasing.

By comparing Fig. 16(a), (b), and (c), it is seen that with 4 natural gas inlets, the natural gas flow velocity is too fast, and the distribution of the area after injection is more concentrated. As a result, it fails to mix with the oxygen sufficiently, leading to insufficient combustion reactions, and there is more oxygen remaining in the roaster. The value of the mass fraction above 2.1 m reached 0.095, which is significantly higher than the number of entrances of the other two. Excessive oxygen residual will result in more heat being used to heat the excess oxygen, resulting in lower heat inside the furnace and affecting the desulfurization process.

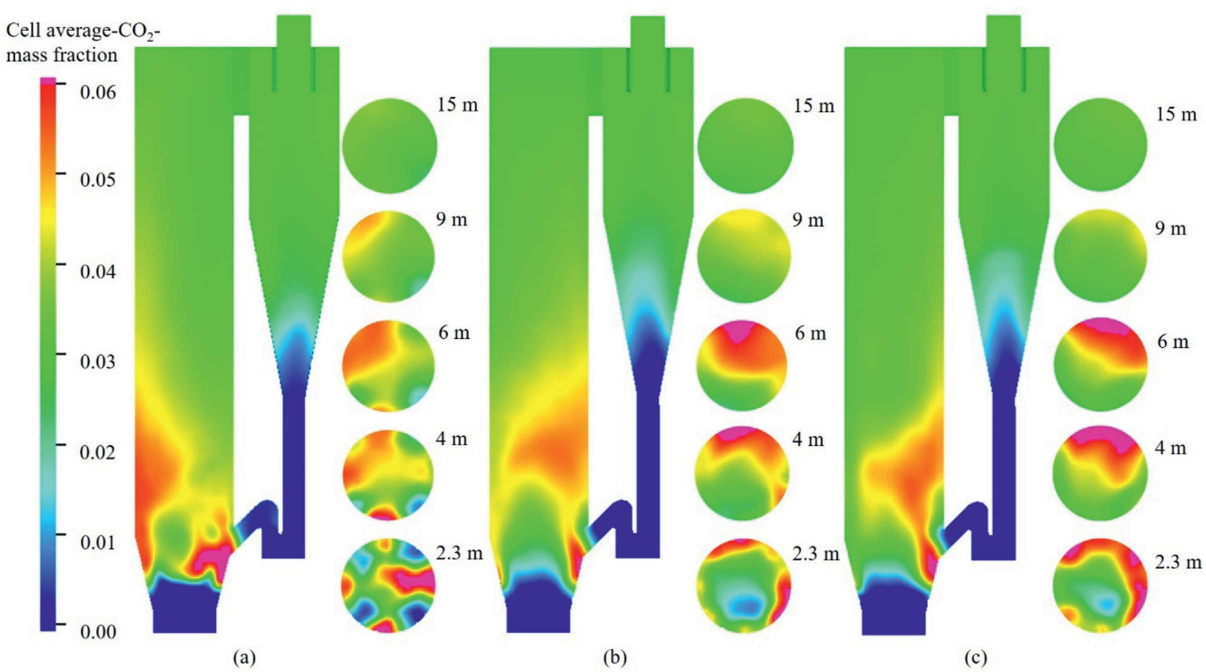

Fig. 14. Distributions of carbon dioxide in the furnace under different numbers of the natural gas inlets: (a) 4, (b) 8, and (c) 12.

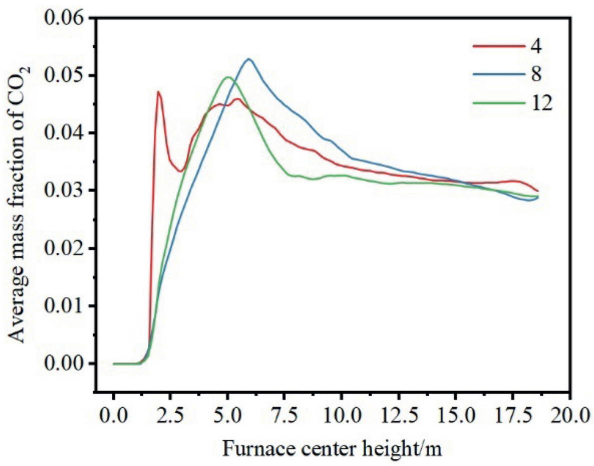

Fig. 15. Distributions of carbon dioxide mass fraction at the center of CFB roaster for different numbers of natural gas inlets.

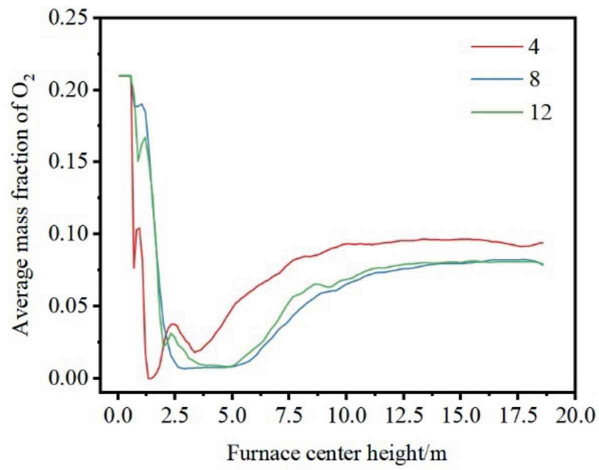

Fig. 17. Distributions of oxygen mass fraction at the center of CFB roaster for different numbers of natural gas inlets.

Fig. 18 shows the distribution of sulfur dioxide in the furnace with different natural gas inlet numbers when the CFB roaster is running stably. The figure shows the mass fraction of sulfur dioxide is the largest in the middle and lower zones of high solid contents, smallest at the return valve.

It is also seen that the sulfur dioxide mass fraction is smaller on the side near the inlet of the return valve because the temperature of the return air flowing into the feeder is lower, which makes the particles on the side close to the return air react more slowly and produce less sulfur dioxide. At the same time, in conjunction with Figs. 18 and 19, the sulfur dioxide distribution fraction is smallest when the number of natural gas inlets is 4 and largest when the number of inlets is 8. It can be inferred that the desulfurization reaction rate is the lowest with 4 natural gas inlets, with 8 natural gas inlets, the desulfurization reaction rate is the highest, natural gas inlets and the desulfurization reaction rate becomes slow again when the number of inlets is increased to 12. The number of natural gas inlets (the flow velocity and distribution of the natural gas) has a significant impact on the rate of desulfurization reaction.

Fig. 19 shows the distribution of sulfur dioxide mass fraction along the center height with different numbers of natural gas inlets when the CFB roaster is running stably. It can be seen that with 4 natural gas inlets, under the isolation of natural gas, sulfur dioxide is formed at the bottom, mass fraction up to 0.26 while with 8 or 12 natural gas inlets, the distribution of sulfur dioxide is more uniform in the direction of the natural gas outlet. Fig. 20 shows the desulfurization efficiency of the roaster after 120 s of operation with different numbers of natural gas inlets. This desulfurization efficiency is calculated by dividing the mass of sulfur dioxide in the flue gas outlet by the mass of sulfur dioxide in the initial bed material. It is seen that with 4, 8 or 12 natural gas inlets, the desulfurization efficiency of the bauxite roasting is 45.3%, 53.8% and 50.4%,

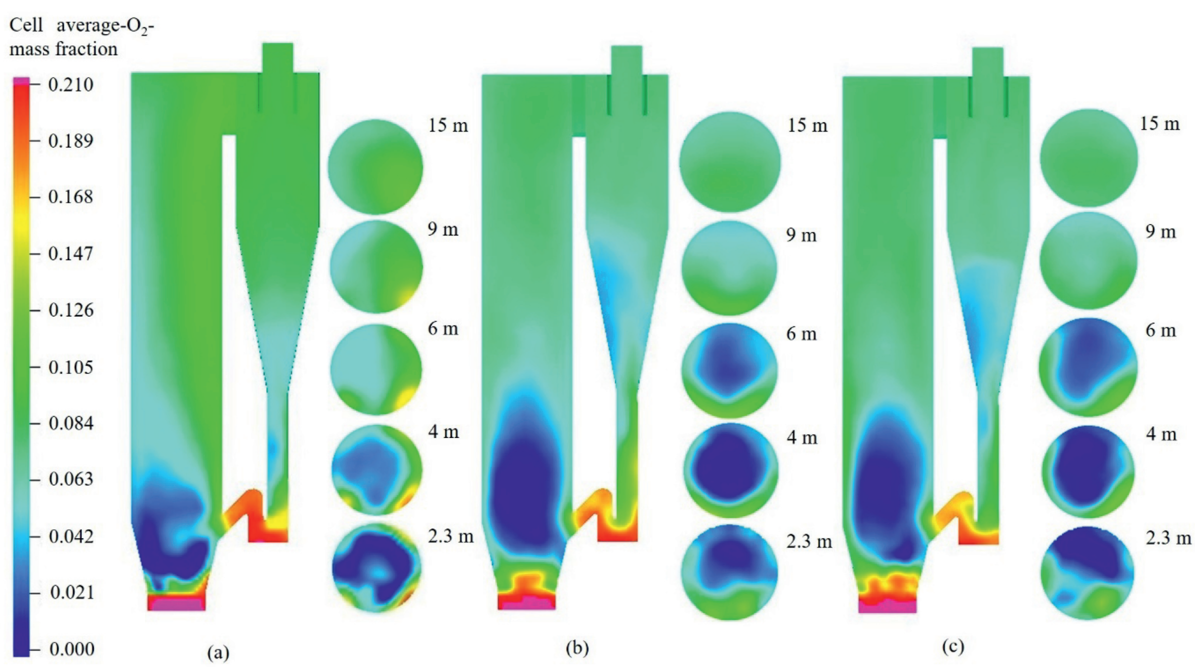

Fig. 16. Distributions of oxygen in the furnace under different natural gas inlet numbers: (a) 4, (b) 8, and (c) 12.

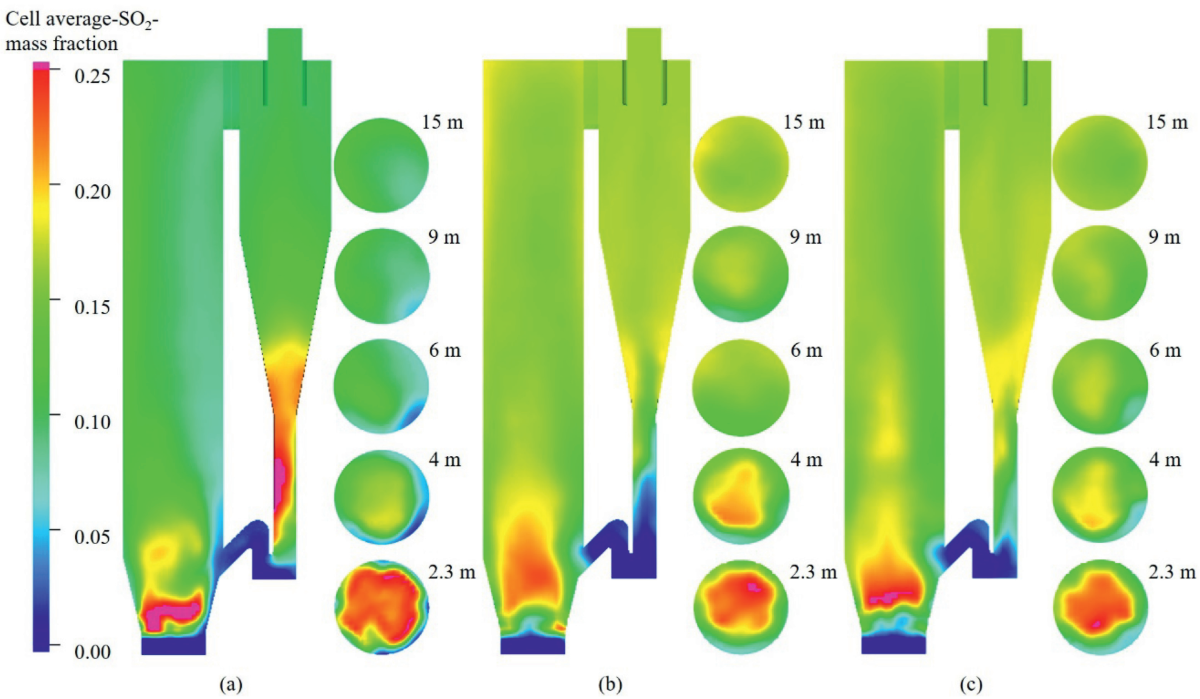

Fig. 18. Distributions of sulfur dioxide in furnace under different natural gas inlet numbers: (a) 4, (b) 8, and (c) 12.

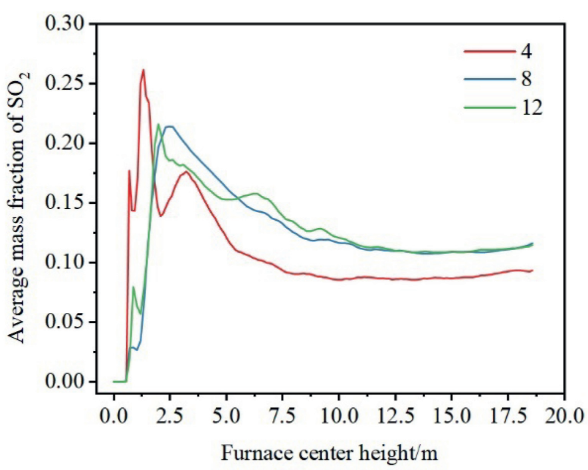

Fig. 19. Distributions of sulfur dioxide mass fraction at the center of CFB roaster for different numbers of natural gas inlets.

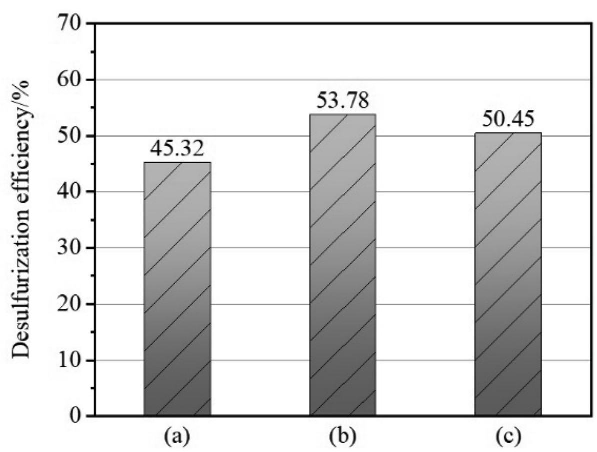

Fig. 20. The desulfurization efficiencies of sulfur dioxide in flue gas after 120 s of operation under different natural gas inlet numbers: (a) 4, (b) 8, and (c) 12.

respectively, and the desulfurization efficiency is best at 53.8% with 8 natural gas outlets, which is 8.5% and 3.3% higher than with the other two numbers of outlets, respectively.

Fig. 21 shows the temperature distribution inside the roaster for different numbers of natural gas inlets. As seen from the figure, the temperature in the lower region of the main furnace is the lowest and the temperature distribution is uneven, the temperature is higher near the wall and lower at the center. The temperature in the middle and lower parts is the highest and uniform. In the cyclone separator, the temperature gradually decreases from the flue gas outlet to the material leg, it is also low at the return valve. This is because air enters the roaster at room temperature. Combined with Figs. 21 and 22, it is seen that when the number of natural gas inlets is 4, the average temperature in the furnace is the lowest, the highest at 8, and lower at 12. Natural gas enters the roaster from the natural gas inlet for combustion, which not only provides heat for the roasting process but also acts as the secondary air. With too few natural gas inlets, the natural gas flow velocity is too fast and blocks the gas–solid rise at the bottom and the gathered particles lead to insufficient gas–solid contact, reduces the efficiency of the combustion reaction, lowering the temperature and thus the efficiency of the desulfurization reaction, this is also the reason for the lower sulfur dioxide mass fraction when the number of natural gas inlets is 4 in Fig. 19. Excessive numbers of natural gas inlets lead to insufficient natural gas penetration and the inability of natural gas to mix uniformly with oxygen in the center of the furnace, which also leads to slow reaction of the bauxites as well as the combustion reaction, resulting in a low furnace temperature and reduced desulfurization efficiency.

According to the simulation results, under the conditions simulated in this paper, the best desulfurization effect and higher

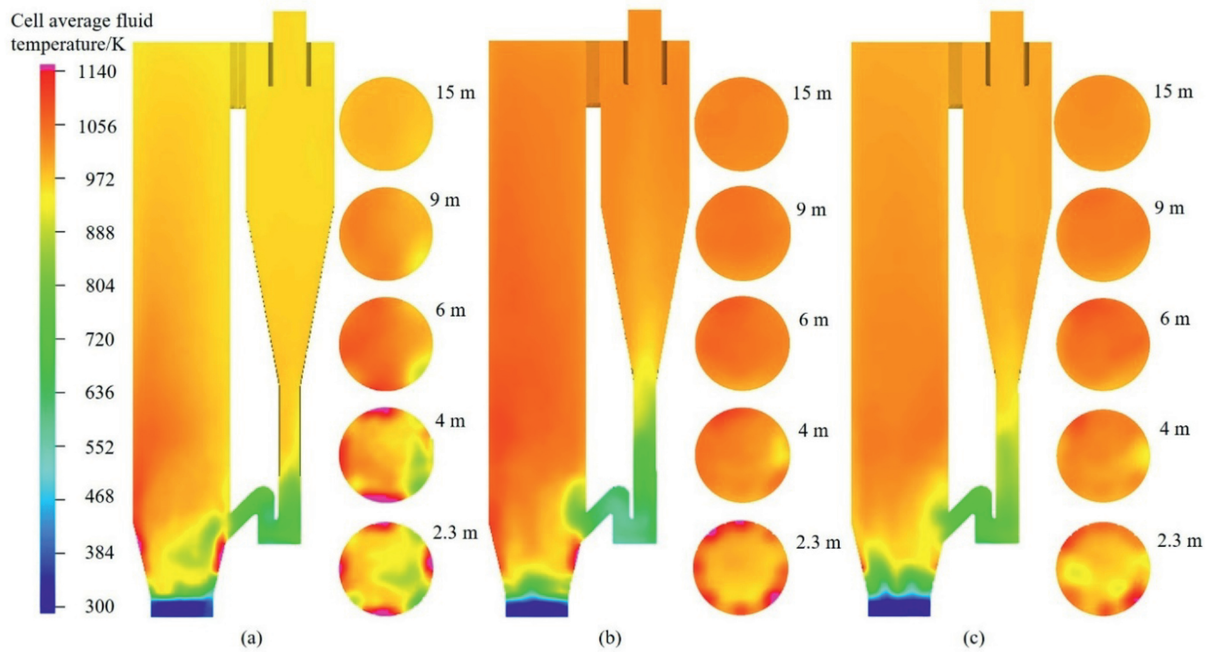

Fig. 21. Temperature distributions of CFB roaster for different number of natural gas inlet number: (a) 4, (b) 8 and (c) 12.

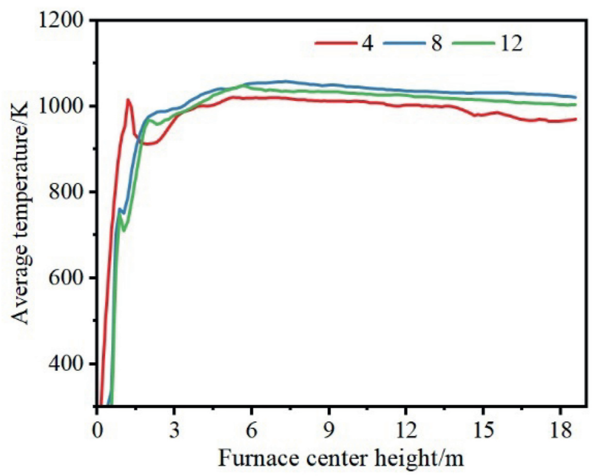

Fig. 22. Temperature distributions at different heights of the main furnace center under different numbers of the natural gas inlets.

temperature in the furnace are achieved when 8 natural gas inlets are selected with the same total natural gas flow.

4. Conclusions

In this work, a circulating fluidized bed with a production capacity of 310 $t \cdot d^{-1}$ for desulfurization of high-sulfur bauxite has been modeled and simulated with a CPFD method. The effects of primary air flow velocity and the number of natural gas inlets on the circulation and desulfurization efficiencies of this roaster have been investigated. By focusing on the distributions of particle velocity, gas species, temperature, and pressure in the CFB roaster under different conditions, the conclusions are as follows:

(1) The primary air flow velocity affects the gas–solid circulation inside the CFB roaster. If the primary air flow velocity is too slow, the particles stay too long and pile up in the main furnace bottom, resulting in uneven gas and solid phase mixing and slowing the desulfurization reaction. If the primary air flow velocity is too fast, too many particles stay in the cyclone separator, resulting in the clogging of the return valve and affecting the gas–solid circulation. The airflow from the return valve also leads to large temperature fluctuations at the bottom of the roaster.

(2) With the same total natural gas flow, 4 inlets make the natural gas flow velocity too large, which hinders the upward movement of the particles at the bottom. 12 inlets make the natural gas flow velocity too small, the natural gas penetration ability is weakened, and the natural gas cannot reach the center of the furnace body, leading to insufficient contact between the gas and the solid and lowering the efficiency of the desulfurization reaction. The desulfurization efficiency is 53.8% with 8 natural gas inlets, which is 8.46% and 3.3% greater than with 4 and 12 inlets, respectively.

In this study, only the internal field of high sulfur bauxite CFB roaster is briefly investigated, and there is still room for improvement of the research content and simulation model. The next step will be to develop internal field details and more studies affecting desulfurization based on a better model.

CRediT Authorship Contribution Statement

Langfeng Fan: Writing – review & editing, Writing – original draft, Visualization, Validation, Methodology, Investigation, Formal analysis, Data curation, Conceptualization. Chengming Xie: Supervision, Formal analysis. Qijin Wei: Supervision. Hongliang Zhao: Writing – review & editing, Visualization, Validation, Supervision, Resources, Project administration, Methodology, Investigation, Funding acquisition, Formal analysis, Data curation, Conceptualization. Rongbin Li: Writing – review & editing, Supervision, Resources, Project administration, Methodology, Formal analysis, Conceptualization. Yongmin Zhang: Software. Fengqin Liu: Writing – review & editing, Supervision, Resources, Project administration, Funding acquisition, Formal analysis, Conceptualization. Hong Yong Sohn: Writing – review & editing, Supervision.

Declaration of Competing Interest

The authors declare that they have no known competing financial interests or personal relationships that could have appeared to influence the work reported in this paper.

Acknowledgements

This study was supported by the National Key Research and Development Program of China (2022YFC2904400) and Guangxi Science and Technology Major Project (GuiKe AA23023033).

Nomenclature

A	area, m^2
A_0	pre-exponential factor
C	constants
D_P	drag function
D	viscosity correlation coefficient
E_{wp}	effective emissivity coefficient
E	activation energy
E_0	activation energy constant
F	frequency of momentum exchange, $m^2 \cdot s^{-1}$
F_{wp}	effective view factor
F_p	friction force of particles, N
g	gravitational acceleration, $m^2 \cdot s^{-1}$
H_{fp}^{C}	enthalpy of reaction
h_f	fluid enthalpy
h	heat transfer coefficient, $W \cdot m^{-1} \cdot K^{-1}$
k_f	fluid thermal conductivity, $W \cdot m^{-1} \cdot K^{-1}$
m_s	solid mass of free carbon per cell volume
m_p	particle mass, kg
P	pressure, Pa
P_s	positive constant
Q	energy source, $J \cdot m^{-3} \cdot s^{-1}$
q	heat flow
r	radius, m
R	molar gas constant
Re	Reynolds number
S_h	conservative energy exchange
T	temperature, K
θ_f	volume fraction
θ_{cp}	particle close pack limit
ρ	density, $kg \cdot m^{-3}$
τ_p	particle stress function, N
ε	a very small constant
u	velocity, $m \cdot s^{-1}$
ϕ	viscous dissipation
β	constant
$\delta \dot{m}_p$	mass source term, $kg \cdot m^{-3} \cdot s^{-1}$

Subscripts

f	fluid phase
p	particle phase
w	wall
d	dense phase
l	lean phase

References

[1] L. Gao, J.H. Li, D.H. Wang, X.Y. Xiong, C.W. Yi, M.Z. Han, Outline of metallogenic regularity of bauxite deposits in China, *Acta Geol. Sin. Engl. Ed* 89 (6) (2015) 2072–2084.

[2] Z.W. Liu, H.W. Yan, W.H. Ma, K.Q. Xie, B.Q. Xu, L.C. Zheng, Digestion behavior and removal of sulfur in high-sulfur bauxite during bayer process, *Miner. Eng.* 149 (2020) 106237.

[3] G. Cheng, J.Q. Zhang, H.H. Su, Z.Y. Zhang, Synthesis and characterization of a novel collector for the desulfurization of fine high-sulfur bauxite *via* reverse flotation, *Particuology* 79 (2023) 64–77.

[4] Y.L. Li, G. Cheng, M.N. Zhang, Y.J. Cao, E. Von Lau, Advances in depressants used for pyrite flotation separation from coal/minerals, *Int. J. Coal Sci. Technol.* 9 (1) (2022) 54.

[5] S. Yuan, H.X. Xiao, T.Y. Yu, Y.J. Li, P. Gao, Enhanced removal of iron minerals from high-iron bauxite with advanced roasting technology for enrichment of aluminum, *Powder Technol.* 372 (2020) 1–7.

[6] G. Cheng, Y.L. Li, M.N. Zhang, Research progress on desulfurization technology of high-sulfur bauxite, *Trans. Nonferrous Metals Soc. China* 32 (10) (2022) 3374–3387.

[7] Z.W. Liu, H.W. Yan, W.H. Ma, P. Xiong, Sulfur removal of high-sulfur bauxite, *Min. Metall. Explor.* 37 (5) (2020) 1617–1626.

[8] Q. Huo, R.Y. Li, C.Q. Chen, C.Q. Wang, T.F. Long, X. Liu, Study on potential microbial community to the waste water treatment from bauxite desilication process, *Environ. Sci. Pollut. Res.* 30 (6) (2023) 15438–15453.

[9] D. Lu, G.Z. Lyu, T.A. Zhang, W.G. Zhang, D. Xie, Y.X. Wang, L. Wang, Roasting pretreatment-low temperature digestion method for comprehensive utilization of high-sulfur bauxite, in: Light Metals 2018, Springer International Publishing, Cham, 2018, pp. 3–8.

[10] C. Tan, C.Y. Chen, J.Q. Li, S.H. Zhang, H.F. Wu, The desulfurization and digestion property of high-sulfur bauxite with coarse-grained particles by roasting: Desulfurization ratio and digestion kinetics, *Trans. Indian Inst. Met.* 75 (7) (2022) 1821–1830.

[11] S.W. Jiu, B. Zhao, Y.X. Chen, High-efficiency desulfurization of high-sulfur bauxite calcined in a conveyor bed: Kinetics, process, and application, *Processes* 10 (8) (2022) 1586.

[12] H.F. Wu, C.Y. Chen, J.Q. Li, Y.P. Lan, L.Z. Wang, B.L. Quan, H.X. Jin, Digestion mechanism and crystal simulation of roasted low-grade high-sulfur bauxite, *Trans. Nonferrous Metals Soc. China* 30 (6) (2020) 1662–1673.

[13] R.F. Wang, S. Yuan, P. Gao, Y.J. Li, Application of suspension magnetization roasting as technology for high-efficiency separation of valuable iron minerals from high-iron bauxite, *Trans. Nonferrous Metals Soc. China* 32 (7) (2022) 2391–2402.

[14] J. Hammerschmidt, J. Güntner, B. Kerstiens, Roasting of gold ore in the circulating fluidized-bed technology, *Dev. Miner. Process.* 15 (2005) 433–453.

[15] M. Siedlecki, W.D. Jong, A.H.M. Verkooijen, Fluidized bed gasification as a mature and reliable technology for the production of bio-syngas and applied in the production of liquid transportation fuels—A review, *Energies* 4 (3) (2011) 1–46.

[16] K.G. Thomas, A.P. Cole, Roasting Developments—Especially Oxygenated Roasting, Elsevier, Amsterdam, 2016, pp. 73–392.

[17] T. Wang, H. Zhang, H.R. Yang, J.F. Lv, Oxidation mechanism of pyrite concentrates (PCs) under typical circulating fluidized bed (CFB) roasting conditions and design principles of PCs' CFB roaster, *Chem. Eng. Process. Process. Intensif.* 153 (2020) 107944.

[18] D.M. Snider, P.J. O'Rourke, M.J. Andrews, Sediment flow in inclined vessels calculated using a multiphase particle-in-cell model for dense particle flows, *Int. J. Multiphas. Flow* 24 (8) (1998) 1359–1382.

[19] D.M. Snider, Three fundamental granular flow experiments and CPFD predictions, *Powder Technol.* 176 (1) (2007) 36–46.

[20] Y.S. Liang, Y.M. Zhang, T.W. Li, C.X. Lu, A critical validation study on CPFD model in simulating gas–solid bubbling fluidized beds, *Powder Technol.* 263 (2014) 121–134.

[21] D. Tskhakaya, K. Matyash, R. Schneider, F. Taccogna, The particle-in-cell method, *Contrib. Plasma Phys.* 47 (8-9) (2007) 563–594.

[22] X. Shen, L. Jia, Y.L. Wang, B.H. Guo, H.D. Fan, X.L. Qiao, M. Zhang, Y. Jin, Study on dynamic characteristics of residual char of CFB boiler based on CPFD method, *Energies* 13 (22) (2020) 5883.

[23] J. Yan, X.F. Lu, R. Xue, J.Y. Lu, Y. Zheng, Y. Zhang, Z. Liu, Validation and application of CPFD model in simulating gas–solid flow and combustion of a supercritical CFB boiler with improved inlet boundary conditions, *Fuel Process, Tech* 208 (2020) 106512.

[24] J. Chang, X.R. Ma, X. Wang, X.H. Li, CPFD modeling of hydrodynamics, combustion and NO_x emissions in an industrial CFB boiler, *Particuology* 81 (2023) 174–188.

[25] H.P. Liu, S.C. Li, X.X. Xiang, S.S. Gong, C.X. Jia, Q. Wang, B.Z. Sun, Simulation of biogas co-combustion in CFB boiler: combustion analysis using the CPFD method, *Case Stud. Therm. Eng.* 59 (2024) 104610.

[26] J. Zhang, Y.M. Li, L. Mei, X.L. Yu, X. Lv, J.P. Wang, J. Yan, R.Y. Sun, Study on the effect of secondary air layout on CO reduction performance in a 75 t/h biomass CFB boiler burning wheat straw, *Energies* 16 (8) (2023) 3312.

[27] X.L. Huang, X.L. Jin, L.X. Dong, R.Y. Li, K.X. Yang, Y.H. Li, L. Deng, D.F. Che, CPFD numerical study on tri-combustion characteristics of coal, biomass and oil sludge in a circulating fluidized bed boiler, *J. Energy Inst.* 113 (2024) 101550.

[28] D.G. Raheem, B. Yılmaz, Ö. Sibel, Comparison of oxygen enriched and oxy-combustion characteristics of lignite in a CFB: Modelling and experimental verification, *Powder Technol.* 389 (2021) 355–367.
[29] Y. Wang, X.Y. Chen, L.P. Xu, M.W. Ma, X.L. Huang, F. Han, Y. Zhou, C. Du, Y.D. Da, L. Deng, Computational particle fluid dynamics simulation on combustion characteristics of blended fuels of coal, biomass, and oil sludge in a 130 $t \cdot h^{-1}$ circulating fluidized bed boiler, *Energies* 17 (1) (2024) 149.
[30] A. Ahmadzadeh, H. Arastoopour, F. Teymour, Numerical simulation of gas and particle flow in a rotating fluidized bed, *Ind. Eng. Chem. Res.* 42 (12) (2003) 2627–2633.
[31] B.H. Lee, K.M. Kim, Y.H. Bae, H.S. Oh, G.B. Kim, C.H. Jeon, Y.H. Ahn, Effect of bed particle size on the gas–particle hydrodynamics and wall erosion characteristics in a 550 MWe USC CFB boiler using CPFD simulation, *Energy* 254 (2022) 124263.
[32] W.P. Adamczyk, P. Kozołub, A. Klimanek, R.A. Białecki, M. Andrzejczyk, M. Klajny, Numerical simulations of the industrial circulating fluidized bed boiler under air- and oxy-fuel combustion, *Appl. Therm. Eng.* 87 (2015) 127–136.
[33] X. Chen, J.C. Ma, X. Tian, J.L. Wan, H.B. Zhao, CPFD simulation and optimization of a 50 kWth dual circulating fluidized bed reactor for chemical looping combustion of coal, *Int. J. Greenh. Gas Control* 90 (2019) 102800.
[34] S.Q. Sia, W.C. Wang, Numerical simulations of fluidized bed fast pyrolysis of biomass through computational fluid dynamics, *Renew. Energy* 155 (2020) 248–256.
[35] F.M. Auzerais, R. Jackson, W.B. Russel, The resolution of shocks and the effects of compressible sediments in transient settling, *J. Fluid Mech.* 195 (1988) 437–462.
[36] D.M. Snider, S.M. Clark, P.J. O'Rourke, Eulerian–Lagrangian method for three-dimensional thermal reacting flow with application to coal gasifiers, *Chem. Eng. Sci.* 66 (6) (2011) 1285–1295.
[37] K. Luo, D. Wang, T. Jin, S. Wang, Z. Wang, J.H. Tan, J.R. Fan, Analysis and development of novel data-driven drag models based on direct numerical simulations of fluidized beds, *Chem. Eng. Sci.* 231 (2021) 116245.
[38] W.C. Yang, Handbook of fluidization and fluid–particle systems, *China Particuology* 1 (3) (2003) 137.
[39] L. Fan, C. Zhu, Principles of Gas–Solid Flows, Cambridge University Press, Cambridge, 1998.
[40] D. Kunii, O. Levenspiel, Fluidization Engineering, second ed., Butterworth-Heinemann, Oxford, 1991.
[41] C.X. Jia, J.W. Li, J.J. Chen, S.S. Cui, H.P. Liu, Q. Wang, Simulation and prediction of co-combustion of oil shale retorting solid waste and cornstalk in circulating fluidized bed using CPFD method, *Appl. Therm. Eng.* 165 (2020) 113574.
[42] S. Kraft, F. Kirnbauer, H. Hofbauer, CPFD simulations of an industrial-sized dual fluidized bed steam gasification system of biomass with 8MW fuel input, *Appl. Energy* 190 (2017) 408–420.
[43] Y. Hong, B. Fegley Jr., The kinetics and mechanism of pyrite thermal decomposition, *Ber, Der Bunsengesellschaft Für Phys. Chem.* 101 (12) (1997) 1870–1881.
[44] M. Samouhos, P. Angelopoulos, G. Pilatos, M. Taxiarchou, S. Papageorgiou, Kinetic study of non-isothermal decomposition of a composite diasporic-boehmitic bauxite, *IOP Conf. Ser. Mater. Sci. Eng.* 123 (2016) 012048.
[45] H.P. Liu, H.W. Sun, Y. Bi, C.X. Jia, L. Zhang, Y.L. Li, H. Qin, Q. Wang, Effect of secondary air on NO emission in a 440 t/h circulating fluidized bed boiler based on CPFD method, *Particuology* 83 (2023) 18–31.
[46] C.M. Xie, R.B. Li, Q.J. Wei, F.Q. Liu, H.L. Zhao, Y.M. Zhang, H.Y. Sohn, Numerical simulation on gas–solid flow during circulating fluidized roasting of bauxite by a computational particle fluid dynamics method, *Particuology* 90 (2024) 179–188.
[47] A. Dutta, P. Basu, An investigation on heat transfer to the standpipe of a circulating fluidized bed boiler, *Chem. Eng. Res. Des.* 81 (8) (2003) 1003–1014.
[48] M.R. Golriz, B. Sundén, A method for temperature measurements in circulating fluidized bed combustors, *Exp. Therm. Fluid Sci.* 9 (3) (1994) 274–282.
[49] J. Lu, X. Lu, H. Liu, H. Wang, H. He, Calculation and analysis of dissipation heat loss in large-scale circulating fluidized bed boilers, *Appl. Therm. Eng.* 30 (13) (2010) 1839–1844.
[50] H.P. Liu, J.W. Li, Q. Wang, Three-dimensional numerical simulation of the co-combustion of oil shale retorting solid waste with cornstalk particles in a circulating fluidized bed reactor, *Appl. Therm. Eng.* 130 (2018) 296–308.
[51] P. Liu, X. Wu, Z.Y. Wang, Y.X. Bo, H.R. Bao, Numerical simulation study on gas–solid flow characteristics and SO_2 removal characteristics in circulating fluidized bed desulfurization tower, *Chem. Eng. Process. Process. Intensif.* 176 (2022) 108974.
[52] Q. Ma, F.L. Lei, Y.H. Xiao, Numerical analysis of operating conditions for establishing high-density circulating fluidized bed by CPFD method, *Powder Technol.* 338 (2018) 446–457.
[53] M. Upadhyay, H.C. Park, J.G. Hwang, H.S. Choi, H.N. Jang, Y.C. Seo, Computational particle–fluid dynamics simulation of gas–solid flow in a circulating fluidized bed with air or O_2/CO_2 as fluidizing gas, *Powder Technol.* 318 (2017) 350–362.
[54] J.H. Yang, H.R. Yang, G.X. Yue, Experimental study on secondary air jet penetration in circulating fluidized bed, *J. Power Eng.* 28 (4) (2008) 509–513. (in Chinese)
[55] W. Zheng, M. Zhang, Y. Zhang, J. Lyu, H. Yang, The effect of the secondary air injection on the gas–solid flow characteristics in the circulating fluidized bed, *Chem. Eng. Res. Des.* 141 (2019) 220–228.
[56] S.-Z. Sun, Z.-Y. Wang, M.-K. Du, H. Chen, Design and experimental study of the centrally-located secondary air of a circulating fluidized bed, *J. Eng. Therm. Energy Power* 25 (1) (2010) 51–56.
[57] X.B. Xiao, H.R. Yang, H. Zhang, J.F. Lu, G.X. Yue, Research on carbon content in fly ash from circulating fluidized bed boilers, *Energy Fuels* 19 (4) (2005) 1520–1525.